Rainfall estimation by combining radar and infrared satellite data for nowcasting purposes

Federico Porcú[1], Marco Borga[2] and Franco Prodi[1,3]

[1] *FISBAT-CNR, Clouds and Precipitation Group, via Gobetti 101, I-40129 Bologna, Italy*
[2] *DTeSAF, University of Padua, Agripolis, I-35020 Legnaro (PD), Italy*
[3] *Physics Department, University of Ferrara, via Paradiso 12, I-44100 Ferrara, Italy*

The aim is to evaluate the use of infrared satellite precipitation estimates for nowcasting purposes in the context of a real-time flood-warning scheme. A radar-based calibration technique is described which is applied to the Negri–Adler–Wetzel scheme. This procedure employs radar data over a defined calibration area to estimate, for each satellite image, actual rain-rates to be used in the Negri–Adler–Wetzel scheme. Calibrated satellite estimates obtained from this procedure can be used to diagnose areas of precipitation beyond radar range, thus allowing an extension of precipitation nowcasting lead time. Calibrated estimates are compared with radar rainfall measurements and results are discussed for various sizes of integration area. Calibration reduces consistently both bias and variance of the error of the original Negri–Adler–Wetzel estimates, even for integration areas as small as 2000 km². This indicates the capabilities of the new technique for nowcasting purposes over medium-sized river basins.

1. Introduction

There is still wide interest in using satellite infrared (IR) and visible (VIS) data for precipitation estimation and monitoring, especially in the context of operational nowcasting applications. Early work in the 1970s and 80s focused mainly on the estimation of climatic scale distributions of principally convective rainfall (Barrett & Martin, 1981). Now opportunities arise to combine satellite IR data with passive microwave satellite data (Levizzani *et al.*, 1996, Adler *et al.*, 1993), ground radar network data (Browning, 1979; Bellon *et al.*, 1980; Cheng & Brown, 1995) and mesoscale and limited area numerical model outputs (Bellerby & Barrett, 1993; Garand & Grassotti, 1995; Huffman *et al.*, 1995) to improve rainfall estimation and very short range precipitation forecasts at space–time scales suitable for on-line flood forecasting.

A number of successful satellite rainfall estimation techniques (Lovejoy & Austin, 1979; Tsonis & Isaac, 1985 among others) make use of both IR and VIS data, in order to improve the definition of the cloud types causing rain. Bi-spectral and IR techniques have been recently compared (King *et al.*, 1995) showing that considerable improvement, with respect to IR-based techniques, can be achieved by using VIS data (i.e. in screening out the cirrus contribution to rain areas). However, owing to the need to monitor precipitation during the night as well as during the day and to avoid spurious biases in estimates, only IR data are used here.

In this paper a procedure is proposed to calibrate METEOSAT IR precipitation estimates by using weather radar rainfall. Radar-calibrated satellite estimates obtained from this procedure can be used to diagnose areas of precipitation beyond radar range, thus allowing an extension of the lead time of precipitation nowcasts. As a preliminary step to the assessment of the proposed calibration procedure, we provide an analysis of two IR-based precipitation estimation techniques: the Negri–Adler–Wetzel (Negri *et al.*, 1984) and the GOES precipitation index (Arkin, 1979; Arkin & Janowiak, 1991), hereafter referred as NAW and GPI, respectively. Performance of the two techniques for rain area delineation is evaluated; furthermore, areal mean precipitation estimates by NAW are compared with radar-based rainfall for various integration areas.

The assessment of the proposed calibration procedure is based on the analysis of three rainfall events that occurred in northern Italy and were driven by an autumnal cold front circulation. These events are representative of a typical meteorological situation which often becomes established over the western Mediterranean in autumn and is characterised by cyclogenesis in the Lion Gulf or surrounding regions. Cold fronts generated by this kind of cyclonic circulation bring humid warm air from the south and/or south-west, developing pre-frontal convective clouds and frontal stratified clouds which affect the northern rugged coastline. As a consequence of heavy rainfalls

generated by such atmospheric conditions, short rivers draining the southern slopes of the Pyrenees, the Alps Maritimes and the Apennines produce intense floods and flash floods which hit the densely populated regions along their courses (Barrett & Mitchell, 1991; Porcú *et al.*, 1997). Nowcasting of precipitation may be very useful for flood forecasting purposes in these areas, where small and medium-size (from 100 to 1000 km²) catchments are concerned. However, the partially stratified characteristics of these events make it difficult to carry out a satellite-based analysis: for example, lower-level forcing that cannot be easily identified from the satellite IR data. These difficulties motivate efforts to establish procedures for satellite calibration by means of radar rainfall estimates.

The proposed radar-based calibration procedure (identified here as the run time calibration technique – hereafter RTC) is based on the NAW and uses radar rainfall estimates to adjust, for every satellite image, the NAW rainfall coefficients. Adjustment is carried out on a calibration area located inside the radar domain.

This paper is organised into sections as follows. The dataset used and processing techniques for both satellite and radar data are presented in section 2. Section 3 provides an assessment of NAW and GPI performances for rain area delineation. Quantitative precipitation estimates obtained by NAW are discussed in section 4. The RTC calibration procedure is described and compared to NAW in section 5. The conclusion is the subject of the last section.

2. Data

The analysis is performed for three events that occurred on 2–4 October 1992, 7–9 October 1993 and 14–15 November 1996 over northern Italy (hereafter OCT92, OCT93 and NOV96, respectively). For these events METEOSAT and Doppler radar data are available. Data from a network of 30 tipping bucket raingauges logged via a data acquisition system are also available.

2.1. Description of events

Some characteristics of the rainfall events, as observed by radar on a 180×140 km² study area centred on the radar location (Figure 1(*a*)), are reported in Table 1. OCT92 and OCT93 are generally characterised by higher rain-rates than for NOV96. From the synoptic point of view, OCT93 and NOV96 have a similar behaviour, since the cyclonic centres develop as a lower-latitude perturbation of a frontal wave related to an higher-latitude depression. For these cases, the cyclogenesis is weak and the lifetime short. OCT92 evolves in a more complex way: the depression is deep and long lasting (more than three days in total). The
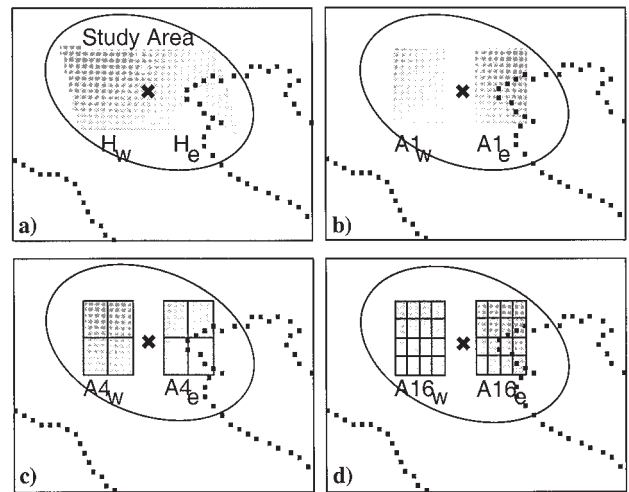

Figure 1. *Location of areas, in grey, used for this study, as seen by the satellite: (a) whole study area and H_e and H_w areas, (b) A1 areas, (c) A4 sub-areas and (d) A16 sub-areas. The radar position (black cross) and range (thin contour) are also shown.*

low centre, which originated over the British Isles, moved southward reaching the Mediterranean in 36 hours and then remained stationary for 36 hours over the Genoa Gulf. Only the second part of this event is considered here because it induced flood conditions over the study area.

2.2. METEOSAT data processing

METEOSAT IR (10.5–12.5 µm) data, extracted from the FISBAT Institute archive, are used for this study. The temporal resolution of the satellite data is 30 minutes, and the spatial resolution of the pixel over northern Italy is about 7.5 km (to the north) by 5 km. During the first two events the satellite was in autumnal eclipse, so the first and last two images were not disseminated. Moreover a few images during all the events were not received. The IR images were converted to temperature using the EUMETSAT calibration coefficients. Rainfall area delineation is accomplished by using GPI and NAW, while only NAW is used for quantitative comparison. GPI and NAW are briefly summarised below.

(a) *GPI.* The GPI delineates rain areas by means of a fixed threshold of 235 K: all the pixels colder that this threshold precipitate at a constant rate of 3 mm h⁻¹. GPI is a broadly accepted standard for IR-only techniques and it is used by the Global Precipitation Climatology Project.

(b) *NAW.* The NAW technique first defines clouds in the IR image by means of the 253 K isotherm. Next, for each area defined as cloud, the coldest 10% is assigned a rain-rate R_{10}, and the next 40% is assigned a lower rain-rate of R_{40}. The warmest 50% cloud fraction is assigned a rain-rate R_{50}, equal to zero in the original setting of the tech-

Table 1. *Description of the selected events*

Event	Beginning of the event	Duration (hh:mm)	Cumulated areal rainfall over the study area (mm)	Min/Max rainfall averaged over the study area (mm h^{-1})	Central pressure of the low (hPa)	Position of the low (lat, long)
OCT92	2 October 1992 21:30 UTC	47:00	74.24	0.18/3.66	990	44.5°N, 8.5°E
OCT93	7 October 1993 21:30 UTC	29:30	49.63	0.03/4.34	1005	48°N, 10°E
NOV96	14 November 1996 02:00 UTC	35:30	14.05	0.00/1.87	1010	44°N, 8°E

nique. This means that the threshold for high and low precipitation assignments may vary for each different type of cloud. The nominal rain-rates have been determined by Negri *et al.* (1984) for tropical thunderstorm events as follows: $R_{50} = 0$, $R_{40} = 2$ and $R_{10} = 8$ mm h^{-1}. Attempts have been made to adapt these values for mid-latitude climate (Levizzani *et al.*, 1990; Marroccu *et al.*, 1993). It was found that a re-calibration of the coefficients allows an improved description of non-tropical events.

For satellite-radar comparison, radar images were remapped, after parallax correction, onto the METEOSAT grid. Since the radar domain is scanned by the satellite approximately at the 22nd and 52nd minute each hour, radar-based reference rain-rates were obtained by appropriately averaging radar maps taken from the 15th to the 30th minute, and from the 45th to the 60th minute, respectively.

Evaluation of rainfall rate estimates at the high spatial and temporal resolution made possible with IR data is a challenging validation problem. Sparse rain-gauge networks present difficulties in delineating rainy areas, especially given the extremely small-scale variability of most rainfall. In this context radar observations of rainfall are generally most useful. However, use of radar rainfall data as reference values for validation of satellite rainfall estimates poses a number of questions, since (a) radar is itself a remote sensing technique with its own unique error sources and calibration problems and (b) the sampling properties of the two devices are vastly different. Satellite estimation cannot be evaluated with confidence unless the validation data set is itself known to be very well calibrated in an absolute sense. For these reasons, radar data processing plays an important part in the assessment of satellite estimates.

2.3. Radar data processing

The radar-derived data sequences selected for the present analysis were provided by the C-band Doppler radar located in northern Italy on Monte Grande hill, close to Venice and Padua. The technical characteristics of the radar are reported in Table 2. The Monte Grande Hill radar is located in a region ranging from the plains of the Po river valley to high-elevation mountains (the north-eastern Italian Alps, with maximum altitude around 2500 m a.s.l.). The complex topography of the mountain area leads to the radar being badly affected by shielding problems which cannot be overlooked. Several radar rainfall error sources are magnified when the rainfall estimation is required over mountainous terrain. The presence of significant relief necessitates the use of radar beam scans for relatively large-elevation tilts in order to minimise the interception of the radar beam with the topography. This increases the height at which the radar observes the atmosphere. Therefore, if either the nature or intensity of the precipitation varies with height, radar indications may not be representative of surface rainfall.

The radar data processing step was designed to incorporate into the radar rainfall estimator as much radar information as possible. Since a detailed description of the radar rainfall estimation scheme is not central to the issue at hand, only a short presentation is given here.

The preliminary data processing step in the rainfall estimation algorithm is an attenuation correction, which is performed using an iterative procedure that is an implementation of the algorithm by Hildebrand (1978). Care was also taken to correct for effects due to the vertical variations in reflectivity caused by melting within the bright band. For this purpose, the algorithm developed by Andrieu & Creutin (1995) was used. This algorithm aims to correct for this kind of error by identifying a function called the vertical profile of reflectivity (VPR). Identification of VPR allows computation of a correction factor function, which depends on the VPR and the radar beam geometry. Correction for VPR influence is achieved by applying the correction factor function to the reflectivity field taken at a given elevation angle. Doing so, the field is corrected to reproduce, on the basis of the identified VPR, the surface reflectivity field. A simulation-based validation of the correction technique in conditions similar to those encountered here is described by Borga *et al.* (1997). Correction for the residual beam blocking was performed taking into account the propagation of the beam in the atmosphere

F Porcú, M Borga and F Prodi

Table 2. *Monte Grande weather radar characteristics*

Parameter	Value
Location	45° 21' 46" N, 11° 40' 25" E, 470 m a.s.l.
Wavelength	5.5 cm
Polarization	linear horizontal
Beamwidth (3dB)	0.9°
Peak power	250 kW
Quantization	256 levels
Bin size	1 km × 0.85°
Elevations	0°30', 1°, 1°30', 2°30', 3°30', 4°30', 6°, 7°30', 10°, 15°
Range	120 km
Update time	15 min

Table 3. *Contingency table for the statistical analysis of the satellite performances in rainfall area delineation*

Observed (radar)	Estimated (satellite)	
	Rain	No rain
Rain	Rr	Rn
No rain	Nr	Nn

and its interaction with the terrain, modelled through a digital terrain model (DTM) characterised by a 200 m by 200 m grid size.

Reflectivity measurements processed in this way are related to the radar rainfall rate through the Marshall–Palmer relation. Radar reflectivity measurements were mapped onto a Cartesian co-ordinate system with a grid spacing of 1 km by 1 km. Each polar data point falling within a Cartesian pixel was used to calculate the mean rainfall rate over the pixel. A similar approach was also applied in the vertical direction. Weather radar volume scans taken at different elevation angles were used to generate approximately vertically constant layer-averaged reflectivity volumes (Bacchi *et al.*, 1996). The layers were set as high as possible to eliminate problems associated with terrain blockage within the radar antenna pattern.

The last step in the radar rainfall estimation algorithm is the mean field bias adjustment. This bias is generated by a number of error sources (such as inappropriate choice of *Z–R* relationship, wrong hardware calibration and wet radome) that produce a systematic bias in the radar estimated rainfall field. The algorithm developed by Smith & Krajewski (1991) has been implemented to estimate the mean field bias by incorporating concurrent rain-gauge measurements. An assessment of the integrated correction procedure has been reported by Borga & Frank (1998)

3. Assessment of rain area delineation

The first step in the validation phase of IR rainfall estimation by GPI and NAW is the assessment of rain area delineation. A contingency table (Table 3) is used to evaluate IR rain area delineation. In the table, observed and estimated values are referred to as radar and satellite observations, respectively. A threshold value of 0.25 mm h^{-1} for radar rainfall is selected to delineate observed rain areas: rain-rates lower than this threshold are not included in the observed rain areas. A contin-

gency table is built for each rainfall event. The following statistics are derived from the table:

Critical success index $$CSI = \frac{Rr}{Rr + Rn + Nr}$$

Probability of detection $$POD = \frac{Rr}{Rr + Rn}$$

False alarm ratio $$FAR = \frac{Nr}{Rr + Nr}$$

Hansen and Kuiper index $$HK = \frac{Rr}{Rr + Nr} + \frac{Nr}{Nr + Nn}$$

Index of symmetry of errors $$ISE = \frac{Rn - Nr}{Rn + Nr}$$

The *CSI* is a severe score because it gives no credit for the correct identification of dry pixels, which are generally in the majority. The range of the *CSI* is 0 to 1, with 1 being a perfect estimation and 0 indicating that no rain pixel was correctly estimated. Estimates with no skill are characterised by *CSI* values slightly more than 0 on average, depending on the precipitation pattern. For instance, in the analysed events no skill diagnosis ranges from *CSI* ≅ 0.3 for OCT92 and OCT93, given the large number of wet pixels in the study area, to *CSI* ≅ 0.2 for NOV96, where observed rainy areas were generally smaller. The range of *POD* and *FAR* is 0 to 1, where 1 indicates a perfect estimation. The *POD* and *FAR* have to be considered together, because a high *POD* could be achieved by estimating precipitation everywhere, but this would result in a large *FAR*. The *HK* score accounts properly for both wet and dry pixels. It ranges from –1 to 1, with 1 being a perfect estimation and –1 a completely incorrect prediction. An estimation with no skill scores 0 on average. Relevance of over/under-estimation effects is measured by the *ISE*. An unbiased estimate scores 0, and *ISE* takes negative (positive) values in case of overestimation (underestimation).

Values of the scores are listed in Table 4 for the three events and for both GPI and NAW. These values are computed for the higher space and time resolution available from satellite data. When examining these scores, one should take into account that rain areas identified by the NAW technique are generally larger

Table 4. *Statistics from the satellite-radar rainfall area comparison for the three events*

Event	Technique	CSI	POD	FAR	HK	ISE
OCT92	GPI	0.58	0.69	0.21	0.47	0.26
OCT92	NAW	0.58	0.71	0.25	0.44	0.10
OCT93	GPI	0.57	0.85	0.34	0.40	−0.52
OCT93	NAW	0.57	0.88	0.39	0.36	−0.64
NOV96	GPI	0.32	0.57	0.58	0.28	−0.39
NOV96	NAW	0.31	0.58	0.60	0.27	−0.34

than those identified by GPI, since it uses a warmer threshold for rain area delineation than GPI (NAW may assign precipitation also to clouds between 253 and 235 K, while GPI does not). This explains why both *POD* and *FAR* scores are greater for NAW than for GPI, while the *ISE* score is smaller. Inspection of results shows that the use of the variable threshold by NAW does not improve rain area delineation in terms of *CSI*, when compared to GPI. The *HK* values are well above zero for each technique for all the events. *ISE* exhibits higher sensitivity to the technique used and to event type with respect to *FAR* and *POD* scores. Inspection of these results shows that rain area is slightly underestimated by both techniques for OCT92, while a more sensitive overestimation is reported for OCT93 and NOV96.

Both techniques perform better for OCT92 and OCT93 than for NOV96. Inspection of satellite images for OCT93 reveals that for some images the study area is completely covered by very cold, precipitating clouds, masking the lower-level cloud structures. This results in an increase of *POD* and *FAR* scores for this event. On the other hand, several radar images for OCT92 and NOV96 are characterised by very light and/or scattered precipitation and by meso-γ structures. The spatial resolution of the IR image is too coarse to represent accurately the spatial variability of rain areas in these cases.

4. Quantitative assessment of NAW precipitation estimates

Instantaneous, IR-derived mean areal precipitation values were computed by using NAW over the study area (see Figure 1) and compared to radar data. Time series of satellite-based mean areal estimates are presented in Figure 2 together with the corresponding radar-based values for the considered events.

Inspection of these time series confirms the fairly good performance of NAW for OCT92. In the first 9 time steps (pre-frontal precipitation) the agreement between satellite and radar is very good, while between time steps 9 and 14 the light and scattered rain is underestimated by the satellite. The successive event of intense stratified precipitation is fairly well described by NAW although slight overestimation (first part) and underes-

timation (last part) are reported. Very strong overestimation characterises satellite estimates for OCT93. This occurs both for the first, prefrontal part (hours 0–8) and for the second part characterised by intense precipitation occurring during the frontal passage. Concerning NOV96, satellite estimation performs quite well during the first cases of light rain, although overestimation is evident around hours 5 and 8. Large overestimation is reported during the second part of the event from time step 20 to the end. It should be noted that this event is characterised by lower rain-rates than the previous ones (see Table 1).

In addition to time series analysis, two error measurements are presented: (a) fractional standard error (*FSE*) and (b) normalised bias (*NBIAS*). These estimates are given by

$$FSE = \frac{\left(\dfrac{1}{N_t} \sum_{i=1}^{N_t} (R_i^r - R_i^s)^2\right)^{1/2}}{\dfrac{1}{N_t} \sum_{i=1}^{N_t} R_i^r}$$

$$NBIAS = \frac{\left(\dfrac{1}{N_t} \sum_{i=1}^{N_t} (R_i^r - R_i^s)\right)}{\dfrac{1}{N_t} \sum_{i=1}^{N_t} R_i^r}$$

where N_t is the number of time steps, R_i^r is the areal mean reference rain-rate value, R_i^s is the corresponding areal mean satellite-based rain-rate value at time step i. Values of the error measures are reported in Table 5 for the three events. The best performance is obtained for OCT92 whilst the worst one is for OCT93. This relates well with the score reported in Table 3 concerning rain area delineation for this event. It should be noted also that OCT93, which gave the highest skill scores for rain area delineation, performs poorly for quantitative estimation of mean areal rainfall.

4.1. Effects of the size of the integration area on Naw performance

The use of satellite-driven precipitation nowcasting techniques for real-time flood forecasting points to the
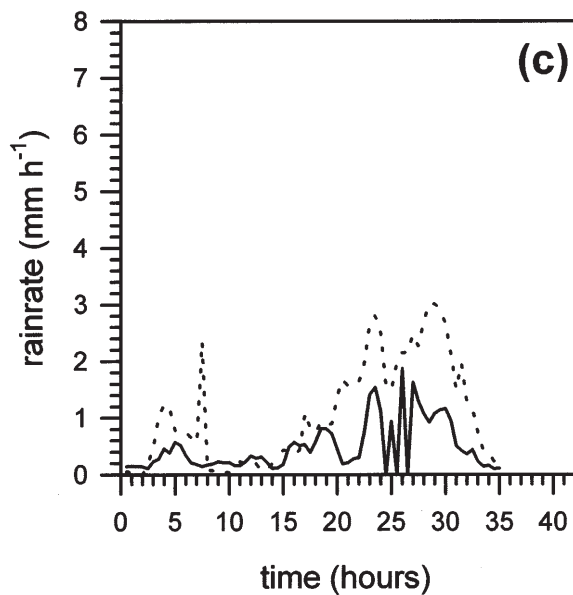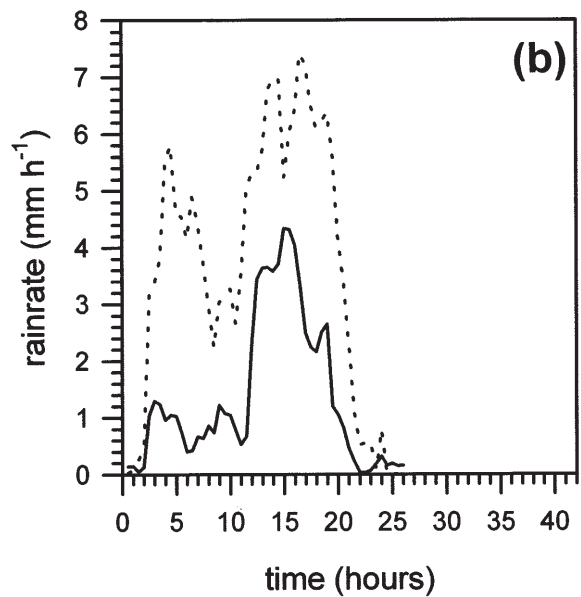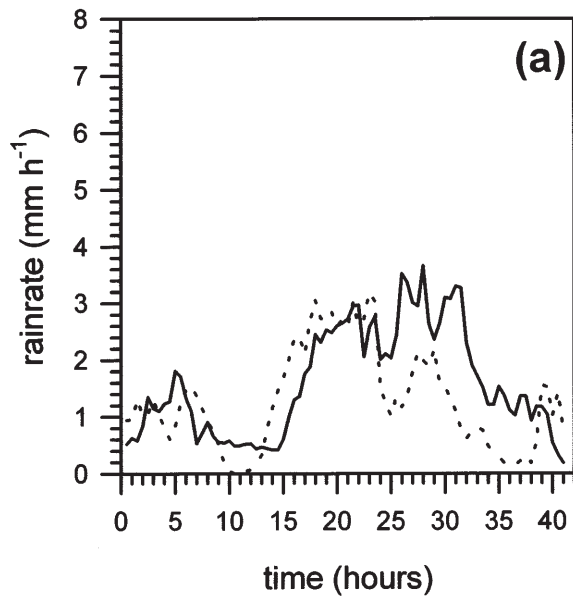
Figure 2. *Mean areal rainfall integrated over the study area estimated by radar (solid line) and NAW (dotted line) for* (a) *OCT92,* (b) *OCT93 and* (c) *NOV96.*

decreased is displayed in Figure 3. These values are obtained by averaging all the *FSE*s corresponding to each area class (e.g. the *FSE* value reported for area A4 is obtained by averaging *FSE*s corresponding to the four areas).

As expected *FSE* increases with decreasing size of the integration areas, especially between A1 and A16. In particular, values of *FSE* corresponding to spatial scales of specific interest for hydrological purposes (around and below 1000 km²) are so high that the use of satellite techniques at these scales appears of very limited quantitative use. For example, *FSE* for OCT93 ranges between 2.4 and 2.8 for A4 and A16. These findings indicate that, for the considered events, NAW cannot determine the distribution of intensity inside the study area with an accuracy suitable for hydrological applications. This points to the need for radar-based calibration if satellite rainfall estimates are to be used for now-casting purposes in the context of flood-forecasting schemes, for events similar to those investigated here.

need for assessing the performance of the techniques at the range of space scales of interest for hydrological applications. Small and medium-scale basins which may benefit from such a type of forecasting range in size from 100 to 1000 km².

To perform such a comparison, we introduce a subdivision of the study area. As shown in Figure 1, the study area is divided into two equal sub-areas H_w and H_e (approximately 12600 km² each), symmetrical with reference to the radar site. In each subarea, areas $A1_w$ and $A1_e$ (≈8000 km² each) are defined in terms of METEOSAT pixels as rectangular regions 16 lines by 12 pixels. Furthermore, each A1 area is divided in four areas A4 (8 by 6, i.e. 2000 km²) and sixteen areas A16 (4 by 3, i.e. 500 km²).

The variation of *FSE* between NAW estimates and reference rainfall when the size of the integration area is

4.2. Consistency of NAW coefficients

Estimation of rainfall by NAW is a two-step procedure: (a) areas with no rain, light and heavy rain are identified for each cloud, and (b) nominal rain-rates are assigned to the selected areas. There is evidence that adjustment of the nominal rain-rates would increase the NAW performances at mid-latitude (Levizzani *et al.*, 1990; Marroccu *et al.*, 1993). The aim of this section is to generalise and validate this statement and delineate a strategy for an automatic reassignment of the nominal coefficients, once the NAW capability to discriminate

Table 5. *Comparison of radar- and satellite-based mean areal rainfall integrated over the study area*

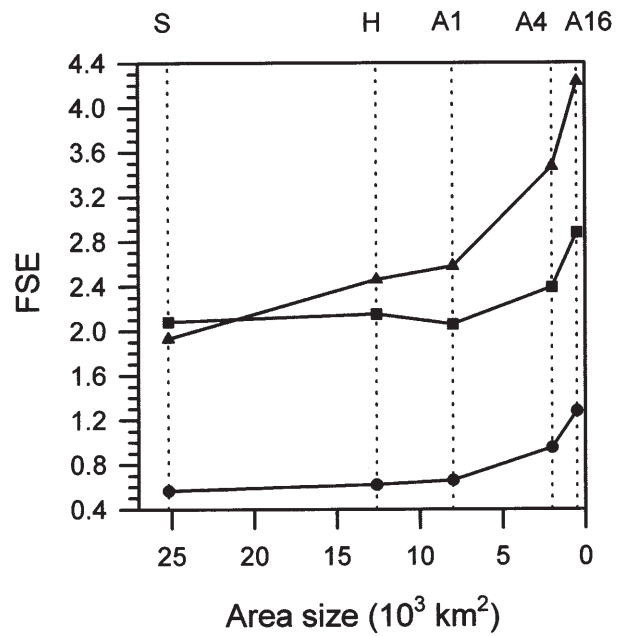| Event	FSE	NBIAS
OCT92	0.57	0.19
OCT93	2.03	−1.68
NOV96	1.93	−1.25

Figure 3. FSE *between NAW and radar rainfall, integrated over areas of decreasing sizes, as a function of the integration areas, for: OCT92 (circle), OCT93 (square) and NOV96 (triangle). Dimensions of the areas are reported on the top axis.*

rain areas into light–moderate and moderate–heavy is assessed.

For the purpose of this assessment, radar rainfall data corresponding to the three satellite rain-rate classes (C_{10}, C_{40} and C_{50}) are analysed. For each C_k ($k = 10$, 40, 50), the following parameters are computed: mean radar rain-rate (m_k); mean radar rainfall over the wet pixels (mz_k); percentage of non-precipitating pixels in each class (z_k); distribution of non-precipitating pixels over the different satellite rain classes (zt_k). Area-averaged values of the parameters are reported in Table 6 for each event.

Inspection of these results shows that the following relations hold for all the three events:

$$m_{50} \, (mz_{50}) < m_{40} \, (mz_{40}) < m_{10} \, (mz_{10})$$

$$z_{50} \, (zt_{50}) > z_{40} \, (zt_{40}) > z_{10} \, (zt_{10})$$

These relations indicate that no-rain, light–moderate and moderate–heavy rain are correctly classified by NAW on average, although a high variance (not reported) affects these mean values. More specifically, inspection of Table 6 reveals that the number of dry pixels decreases from C_{50} to C_{10}, while rain-rate mean values of the wet pixels increase when moving in the same direction.

Distribution of z and zt among the rain classes confirms this analysis, although both exhibit significant variations. Analysis of OCT92 shows that 73% of dry pixels are correctly found in C_{50}, 26% in C_{40} and only 1% in the higher-precipitation class (C_{10}). NOV96 is characterised by similar figures. In OCT93 only 49% of dry pixels are correctly assigned, while the rest are shared between C_{40} (30%) and C_{10} (21%).

Relatively high values are found for m_{50} and for mz_{50}

for OCT92. This is clearly related to the overall underestimation already revealed by the *ISE* score in Table 4 and by the fairly low value of z_{50} in Table 6 for this event. On the other hand, for rainfall events where NAW rain area delineation overestimates the actual precipitation pattern (as for OCT93 and NOV96), m_{50} and mz_{50} are generally low, while z_{50} is very high. However, it is worth noting that values reported for z_{10} for OCT93 and NOV96 are quite high, particularly for the last event. This explains, at least partially, the relatively high values of *FAR* reported in Table 4 for these events.

Values reported for the m coefficients are highly variable among the various events, ranging from 1.9 (NOV96) to 3.1 (OCT92) for m_{10}, and from 0.6 (NOV96) to 2.4 (OCT92) for m_{40}. These values are quite far from those assigned in the original version of NAW (particularly for C_{10}), accounting for the different dynamics of these precipitating systems with respect to those observed by Negri *et al.* (1984) for the original set up of the technique. These differences

Table 6. *Parameters for evaluation of the three NAW rain classes* (C_{50}, C_{40} and C_{10}) *over the study area*; m *and* mz *in mm h^{-1}*, z *and* zt *as percentages*

Event	m_{50}	m_{40}	m_{10}	mz_{50}	mz_{40}	mz_{10}	z_{50}	z_{40}	z_{10}	zt_{50}	zt_{40}	zt_{10}
OCT92	0.7	2.4	3.1	2.3	3.3	3.4	69	26	11	73	26	1
OCT93	0.2	1.1	2.6	1.1	2.1	3.6	81	50	29	49	30	21
NOV96	0.3	0.6	1.9	1.3	1.8	3.0	82	64	39	69	28	3

explain also the high values of *FSE* reported above for NAW in the previous section. The variability of the *m* coefficients indicates also that any reassignment of nominal rain-rates for NAW can hardly cope with the variability among the various cases, as far as these events are considered.

The capability of NAW to correctly separate rain areas into light–moderate and moderate–heavy (as suggested by the correct ranking of *m* and *mz* values among the NAW rainfall classes) is preserved in some way also when the integration area is reduced (results not shown here): for areas H and A1 the ranking still holds, while for areas A4 and A16 exceptions are found.

5. Satellite calibration by means of radar measurements

The findings of section 4.2 provide a basis for a continuous and automatic calibration of NAW coefficients without a posteriori knowledge of the ongoing event, thus allowing its use for nowcasting applications. The proposed radar-based satellite technique requires that a calibration area is defined inside the radar domain. The RTC includes the following steps:

(a) for each satellite image NAW processing is carried out for the calibration area, obtaining cloud partition in the three classes C_{50}, C_{40} and C_{10};
(b) the m_{50}, m_{40} and m_{10} parameters are computed for the calibration area;
(c) these values are used as nominal rain-rates in the NAW processing;
(d) m_{50}, m_{40} and m_{10} are updated every satellite image (half an hour).

5.1. Assessment of RTC

Assessment of the results obtained by RTC is carried out by comparing calibrated satellite estimates and reference rain-rate on an independent target area, which is not included in the calibration area. As a first application of the technique, we consider the areas H_w and H_e previously defined: first H_w (H_e) is used as calibration area and then H_e (H_w) is used as validation area. As an example, for the three events, time series of areal mean reference rainfall obtained for the validation area H_w are compared with NAW estimates in Figures 4(*a*)–(*c*), and with RTC estimates in Figures 4(*d*)–(*f*).

Analysis of these figures shows that RTC improves only marginally over NAW for OCT92. In this case NAW performances are fairly accurate and the calibration only reduces the underestimation between time steps 24 and 35. RTC is more effective for OCT93, reducing the large overestimation of the NAW. A typical advective effect of the calibration procedure is observed in this event: the precipitation peak around

time step 13 is shifted forward by the RTC for about 2.5 hours. This shifting can be explained by observing that the motion of the cloud system is eastward in the concerned period. In these conditions, RTC calibrates the coefficients over H_w, already covered by the major cloud system, and applies the correction instantaneously over H_e, where minor cloud systems were present. In general terms, application of RTC to NOV96 significantly reduces NAW overestimation, even though for the more intense rainfall spells (hours 23–33) RTC is unable to improve the agreement with reference rainfall.

Values of *FSE* and *NBIAS* computed for area H_w using NAW and RTC are reported in Table 7 for the three events. Inspection of these values shows that application of RTC consistently improves satellite estimates: reduction of *FSE* ranges from 23% (OCT92) to 79% (OCT93), while *NBIAS* is lowered in the range from 95% (OCT93) to 25% (NOV96). As expected, better agreement is exhibited for OCT92 and OCT93, where the satellite bias is reduced. For NOV96 the *FSE* reduces as well, but, owing to the low rain-rate, large errors still remain, as indicated by the *NBIAS* value, which highlights a substantial underestimation. This is confirmed also by Figure 4(*f*). The characteristics of this rain event, dominated by light rain episodes which prevent even a rough delineation of rain areas (Table 4), explain the poor performance reported for RTC in this case.

It should be recognised that the correlation in space of the rainfall field at the various spatial aggregation scales implies some dependence between the rainfall characteristics over the calibration and validation area. However, we maintain that results obtained through the validation procedure preserve their representativity, since the RTC technique is aimed at diagnosing areas of precipitation that are beyond radar range but are close to the calibration area.

5.2. RTC application over areas of different sizes

To evaluate the influence of reduction of integration area on RTC performance, the analysis reported in section 4.1 is carried out here using the area subdivision delineated in Figure 1. The assessment is accomplished as follows: first, satellite estimates are calibrated over area H_e (H_w), and then comparison of RTC and reference rainfall is accomplished over west (east) areas A1, A4 and A16. Then the assessment procedure is repeated by using area $A1_e$ ($A1_w$) as the calibration area and comparing RTC and radar rainfall over the west (east) side at the various scales of spatial integration. The interest in evaluating the influence of the reduction of the calibration area is motivated by the need to adjust this area taking into account possible radar error sources (i.e. low-level bright band), which may reduce the quantitative radar range. For each scale of spatial integration, mean values of *FSE* are computed and
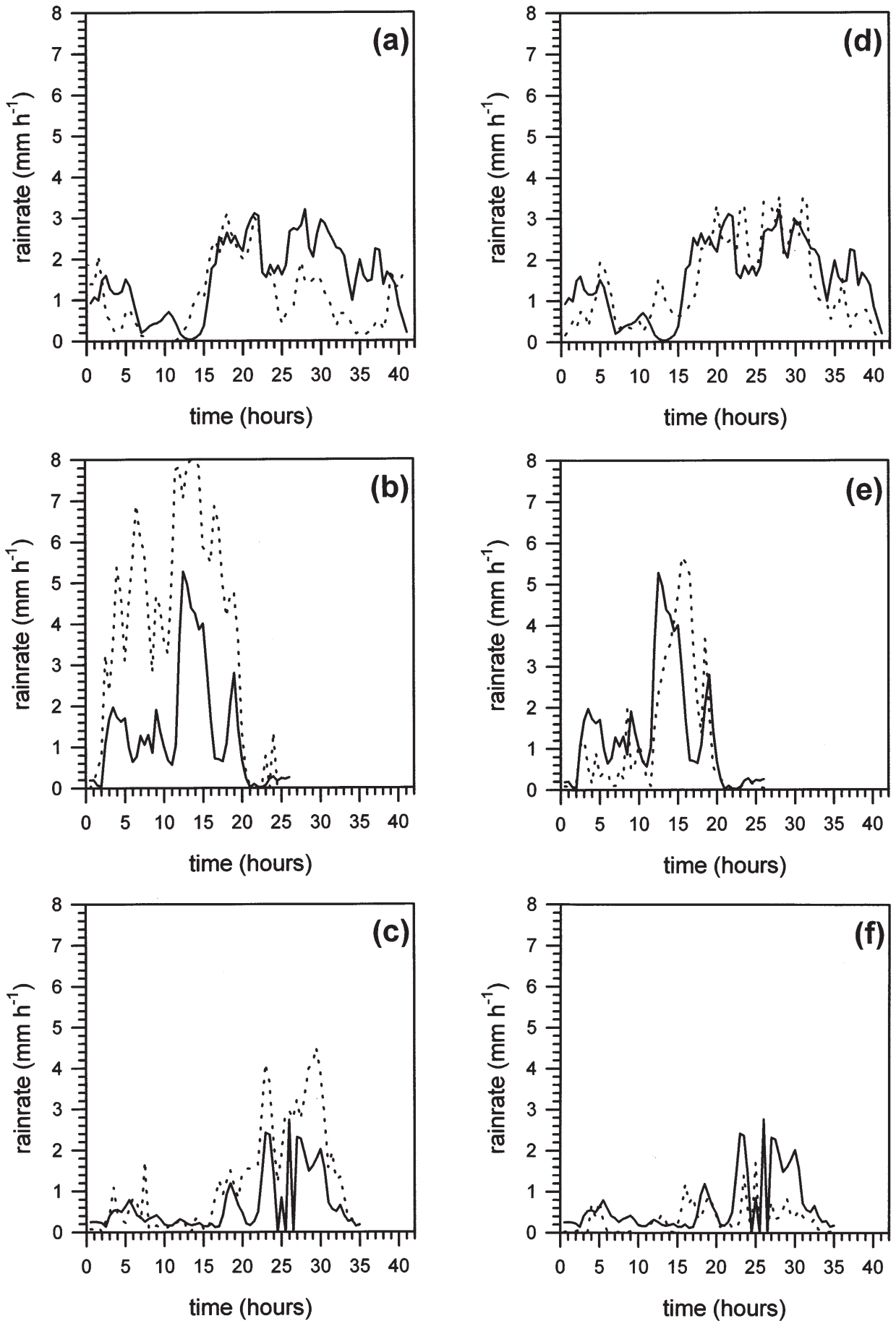
Figure 4. *Mean areal precipitation integrated over the H_w area: on the left computed by radar (solid line) and NAW (dotted line), and on the right computed by radar (solid line) and RTC (dotted line) for (a) & (d) OCT92, (b) & (e) OCT93 and (c) & (f) NOV96.*

F Porcú, M Borga and F Prodi

Table 7. *Validation on H_w area: FSE and NBIAS for NAW and RTC (RTC calibrated on H_e)*

Event	FSE		NBIAS	
	NAW	RTC	NAW	RTC
OCT92	0.61	0.47	0.33	0.07
OCT93	2.23	0.97	−1.71	0.08
NOV96	1.08	0.79	−0.71	0.53

Figure 5. FSE *values between NAW and radar (circles), RTC calibrated over A1 and radar (squares) and RTC calibrated over H and radar (triangles) as a function of the different target area sizes, for OCT92 (dashed), OCT93 (solid) and NOV96 (dotted). Dimensions of the integration areas are reported on the top axis.*

reported in Figure 5 as a function of the size of validation area. It should be noted from Figures 1(b)–(d) that the calibration and validation areas are placed at various distances, particularly when A16 areas are considered. Here the problem of the influence of the calibration/validation area distance on the RTC performance is not directly investigated, but it is clear that it deserves a specific analysis for operational implementation of the procedure.

Analysis of Figure 5 shows that application of RTC leads to a reduction in *FSE* for all three cases and for every validation/calibration area choice. Using H_w as the calibration area, RTC is able to greatly reduce *FSE* and *NBIAS* also integrating over smaller areas, but the achieved error values are still not useful for direct quantitative use: for the smallest area tested in this work (A16 ≈ 500 km²) *FSE* ranges from 1.20 (OCT92) to 3.2 (NOV96). The improvement is more significant for OCT93 and NOV96 than for OCT92. NAW and RTC behave in a similar way when reducing the integration area. Owing to the lower precipitation rate of NOV96, RTC application for this event is more sensitive to integration area size. It should be noted also that the sensitivity of RTC with respect to the variation of calibration area appears to be quite low, although a larger calibration area insures lower *FSE* values for the three cases, as expected.

Figure 6 reports *NBIAS* and *FSE* values concerning A16 areas for the three events, respectively, and for both RTC and NAW. This is to analyse the behaviour of the two techniques on the smallest areas we tested and to provide information on the distribution of the individual *FSE* values, which are averaged in Figure 5. Inspection of these figures shows that *FSE* increases with negative values of *NBIAS*, i.e. overestimation is responsible for the increased errors. A few more specific remarks follow:

(a) RTC is very effective in reducing *FSE* and *NBIAS* for the worst situations, while estimates characterised by relatively low values of *FSE* and *NBIAS* remain generally unaltered;
(b) RTC reduces the variance of the *FSE* and *NBIAS* distributions;
(c) for OCT93 and particularly NOV96 RTC greatly reduces the satellite overestimation but introduces a slight underestimation.
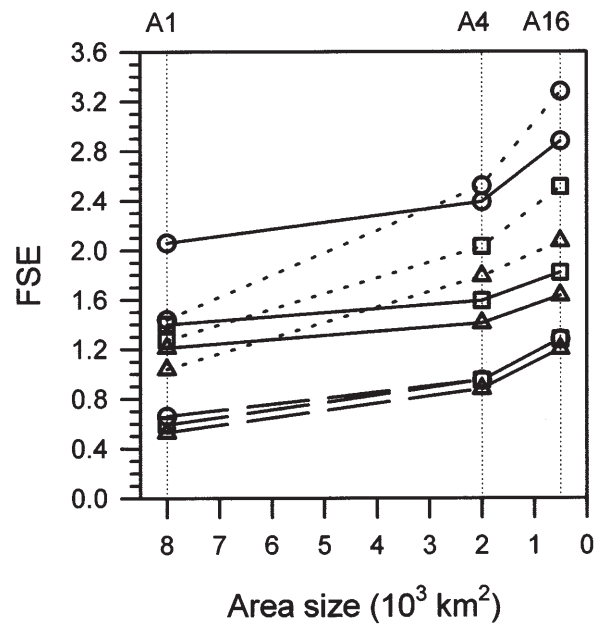
298

6. Conclusion

Rainfall estimates obtained from radar and IR satellite data have been compared for three cyclonic precipitation events over northern Italy. These events were related to cold fronts overpassing the Italian peninsula, and the precipitation was basically stratiform with embedded convection. Two precipitation events (OCT92 and OCT93) were characterised by high rain-rates and induced flooding conditions; in the third case (NOV96), lower rain-rates were measured. The comparison was carried out over a study area 25200 km² in area, where radar data were corrected for a number of error sources (including attenuation, orographic occlusion and effects related to the vertical profile of reflectivity) and adjusted by means of a dense rain-gauge network in order to provide reference fields for the comparison effort.

For the two heavy-rainfall cases, the two IR techniques used (NAW and GPI) show skill factors comparable to those reported in the literature as regards the rain area delineation capability. For the low-precipitation case the performance of the two techniques is lower owing to the presence of light rain, which is difficult to capture with IR satellite data. No significant improvement is achieved using the double threshold method (NAW) compared to the single threshold technique (GPI). This points out clear limitations in the use of the IR satellite channel to monitor stratiform precipitation; also, it appears that these limitations are not related to the processing technique.
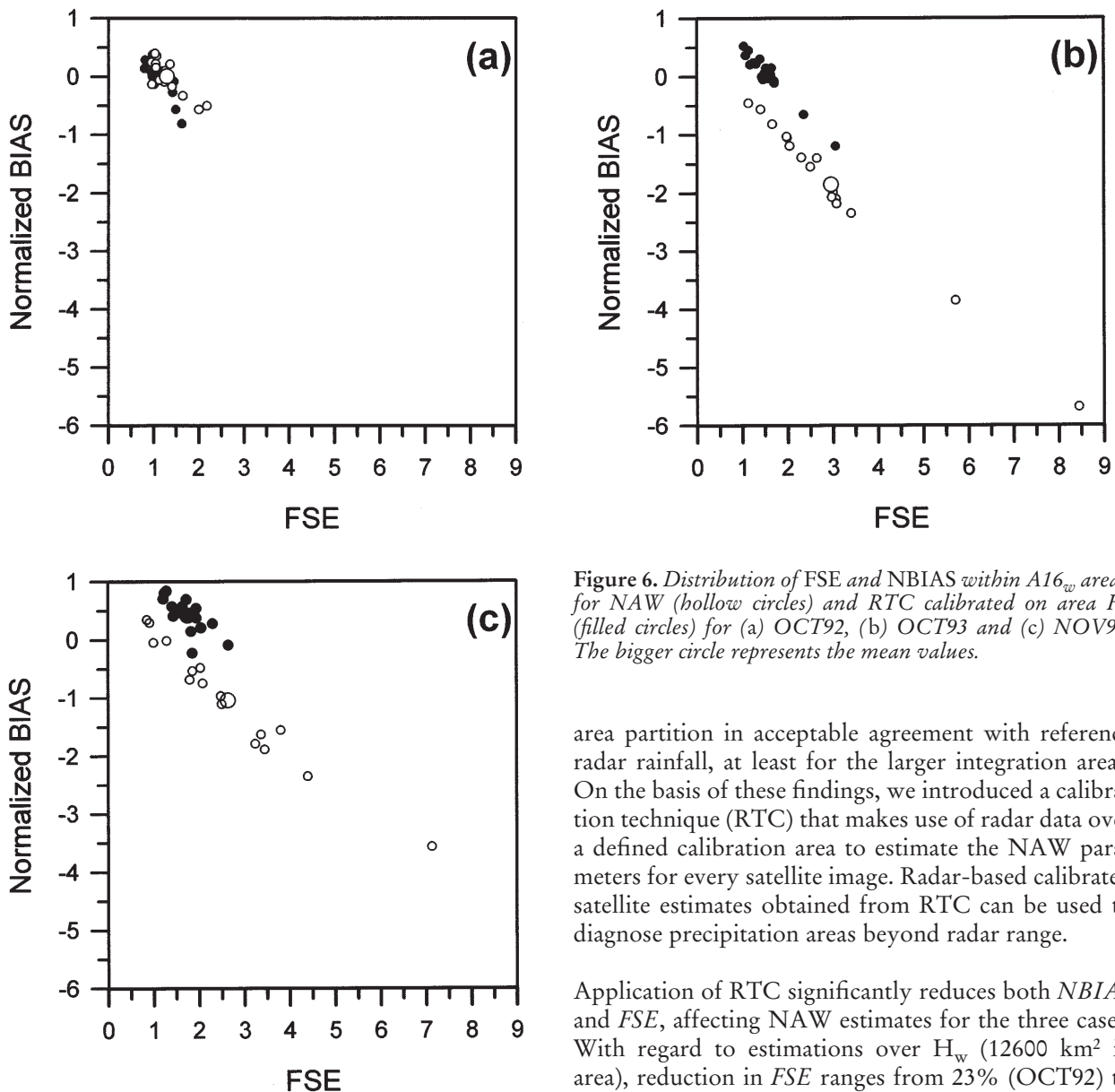
Figure 6. *Distribution of* FSE *and* NBIAS *within A16$_w$ areas, for NAW (hollow circles) and RTC calibrated on area H$_e$ (filled circles) for* (a) *OCT92,* (b) *OCT93 and* (c) *NOV96. The bigger circle represents the mean values.*

Quantitative analysis of the NAW results has been carried out on the study area and selected sub-areas, to test the performance of the technique with respect to the integration area size. Results from this analysis indicate that large discrepancies arise in terms of fractional standard error and normalised bias between radar and satellite even for the largest integration area. For OCT93 and NOV96 large overestimation is reported. This leads to *FSE* values around 2 and 1.3, respectively, for estimates integrated over the whole study area, while for OCT92 *FSE* is around 0.6. *FSE* values increase with a decrease in the integration area: for instance *FSE* for NOV96 reaches 2.5 for integration areas below 2000 km². These findings point out the need for radar-based calibration if satellite estimates are to be used for short-range precipitation forecasting for small to medium-size basins.

Analysis of the cloud partition scheme used by NAW indicates that this technique performs no/low/high rain

area partition in acceptable agreement with reference radar rainfall, at least for the larger integration areas. On the basis of these findings, we introduced a calibration technique (RTC) that makes use of radar data over a defined calibration area to estimate the NAW parameters for every satellite image. Radar-based calibrated satellite estimates obtained from RTC can be used to diagnose precipitation areas beyond radar range.

Application of RTC significantly reduces both *NBIAS* and *FSE*, affecting NAW estimates for the three cases. With regard to estimations over H$_w$ (12600 km² in area), reduction in *FSE* ranges from 23% (OCT92) to 79% (OCT93), while *NBIAS* is lowered in the range from 95% (OCT92 and OCT93) to 25% (NOV96). With regard to rainfall estimation for smaller areas, a considerable reduction of error is still achieved by RTC. However, the residual error is likely to prevent a direct quantitative use of these estimates: for the smallest area tested in this work (A16 ≈ 500 km²) *FSE* ranges from 1.20 (OCT92) to 2.07 (NOV96).

Overestimation, responsible for high NAW errors, is reduced by the calibration procedure for the three cases. Findings concerning the smallest area investigated indicate that the most reliable NAW estimates (those marked by low values of *FSE* and *NBIAS*) are generally unaffected by application of RTC. On the other hand, RTC is very effective in reducing *FSE* and *NBIAS* for the worst NAW estimates. It is clear that a fundamental obstacle to the potential improvement induced by RTC is related to errors in rain area delineation. RTC is still not able to detect precipitation from warmer clouds (above 253 K) and small-scale precipitation patterns. Furthermore, orographic enhancement of

299

precipitation is not resolved by the RTC technique. On-going investigation is focused on the analysis of the capability of the proposed technique in areas characterised by rugged orography.

Better performance of RTC should be achieved when the same cloud system covers both calibration and target areas, as may occur for the large cloud bands related to autumnal cold fronts. For this reason, application of RTC to smaller-scale, convective cloud systems is not envisaged. These encouraging results suggest that additional events should be collected and analysed to further test the calibration procedure. Also, there is need to quantify the effects of discrepancies between reference and calibrated satellite rainfall estimates on discharge predictions for various spatial scales.

Acknowledgements

References

Adler, R. F., Negri, A. J., Keehn, P. R. & Hakkarinen, I. M. (1993). Estimation of monthly rainfall over Japan and surrounding waters from microwave and geosynchronous IR data. *J. Appl. Meteorol.*, **32:** 335–356.

Andrieu, H. & Creutin, J. D. (1995). Identification of vertical profiles of radar reflectivities for hydrological applications using an inverse method. Part 1: Formulation. *J. Appl. Meteorol.*, **34:** 225–239.

Arkin, P. A. (1979). The relationship between fractional coverage of high clouds and rainfall accumulations during GATE, over the B-scale array. *Mon. Wea. Rev.*, **107:** 1382–1387.

Arkin, P. A. & Janowiak, J. (1991). Analysis of the global distribution of precipitation. *Dyn. Atmos. Oceans*, **16:** 5–16.

Bacchi, B., Ranzi, R. & Borga, M. (1996). Statistical characterization of spatial patterns of rainfall cells in extratropical cyclones. *J. Geophys. Res.*, **101 D21:** 26277–26286.

Barrett, E. C. & Martin, D. W. (1981). *The Use of Satellite Data in Rainfall Monitoring*. Academic Press, 340 pp.

Barrett, E. C. & Michell, J. (1991). Satellite remote sensing of natural hazards and disaster in the Mediterranean region. In *Current Topics in Remote Sensing* (Barrett, E. C., Browning, K. A. & Michallef, A., editors), pp 51–67. Gordon and Breach.

Bellerby, T. J. & Barrett, E. C. (1993). Progressive refinement: a strategy for the calibration by collateral data of short-period satellite rainfall estimates. *J. Appl. Meteorol.*, **32:** 1365–1378.

Bellon, A., Lovejoy, S. & Austin, G. L. (1980). Combining satellite and radar data for the short-range forecasting of precipitation. *Mon. Wea. Rev.*, **108:** 1554–1566.

Borga, M., Anagnostou, E. N. & Krajewski, W. F. (1997). A simulation approach for validation of a brightband correction method. *J. Appl. Meteorol.*, **36:** 1507–1518.

Borga, M. & Frank, E. (1998): On the use of radar rainfall estimates for flood simulation in mountainous basins. In *Proc. Second Expert Meeting of the RIBAMOD Concerted Action: Integrated Systems for Real-time Flood Forecasting and Warning*, 'Dino Tonini' International Centre of Hydrology, Monselice, Padua, Italy, 25–26 September 1997, European Commission, 12pp.

Browning, K. A. (1979). The FRONTIERS plan: a strategy for using radar and satellite imagery for very-short-range precipitation forecasting. *Meteorol. Mag.*, **108:** 161–184.

Cheng, M. & Brown, R. (1995). Delineation of precipitation areas by correlation of visible and infrared data with radar data. *Mon. Wea. Rev.*, **123:** 2743–2757.

Garand, L. & Grassotti, C. (1995). Toward an objective analysis of rainfall rain-rate combining observations and short-term forecast model estimates. *J. Appl. Meteorol.*, **34:** 1962–1977.

Hildebrand, P. H. (1978). Iterative correction for attenuation of 5 cm radar in rain. *J. Appl. Meteorol.*, **17:** 508–513.

Huffman, G. J., Adler, R. F., Rudolf, B., Schneider, U. & Keehn, P. R. (1995) A technique for combining satellite-based estimates, raingauge analysis, and NWP model precipitation information into global precipitation estimates. *J. Climate*, **8:** 1284–1295.

King, P. W. S., Hogg, W. D. & Arkin, P. A. (1995). The role of visible data in improving satellite rain-rate estimates. *J. Appl. Meteorol.*, **34:** 1608–1621.

Levizzani, V., Porcú, F. & Prodi, F. (1990). Operational rainfall estimation using METEOSAT infrared imagery: an application in Italy's Arno river basin. Its potential and drawbacks. *ESA J.*, **14:** 313–323.

Levizzani, V., Porcú, F., Marzano, F. S., Smith, E. A. & Prodi, F. (1996). Investigating SSM/I microwave algorithm to calibrate METEOSAT instantaneous rain-rate estimates. *Meteorol. Appl.*, **3:** 5–17.

Lovejoy, S. & Austin, G. L. (1979). The delineation of rain areas from visible and IR satellite data for GATE and midlatitudes. *Atmosphere-Ocean*, **17:** 77–92.

Marroccu, M., Pompei, A., Dalu, G., Liberti, G. L. & Negri, A. J. (1993). Precipitation estimation over Sardinia from satellite infrared data. *Int. J. Remote Sensing*, **14:** 115–134.

Negri, A. J., Adler, R. F. & Wetzel, P. J. (1984). Rain estimation from satellite: an examination of the Griffith–Woodley technique. *J. Climate Appl. Meteorol.*, **23:** 102–116.

Porcú, F., Prodi, F., Franceschetti, S. & Pasetti, S. (1997). Short term climatology of cloud systems leading to flood events in Europe (1991–1996), in Proc. *1997 EUMETSAT Meteorological Satellite Data Users' Conference*, 461–466, EUMETSAT, Darmstadt, EUM P 21.

Smith, J. A. & Krajewski, W. F (1991). Estimation of mean field bias of radar rainfall estimates. *J. Appl. Meteorol.*, **30:** 397–412.

Tsonis, A. A. & Isaac, G. A. (1985). On a new approach for instantaneous rain area delineation in the midlatitudes using GOES data. *J. Climate Appl. Meteorol.*, **24:** 1208–1218.